Power dissipation and impedance measurements in radio-frequency discharges

N. Spiliopoulos, D. Mataras, and D. E. Rapakoulias
Laboratory of Plasma Chemistry, Department of Chemical Engineering, University of Patras, P.O. Box 1407, 26500 Patras, Greece

(Received 11 January 1996; accepted 13 May 1996)

An improved method for the measurement of the power consumed in low pressure, radio frequency discharges is presented. The method involves the measurement of current and voltage waveforms outside the reactor, and the determination of the discharge impedance and the network of parasitics. The measured waveforms are transformed to the equivalent ones at the powered electrode, by using an electrical circuit model of the stray impedance of the cell, with experimentally determined components. A tunable shunt circuit is used for minimizing displacement currents. The equivalent circuit contains elements which account also for resistive power losses in the cell-shunt circuit. The obtained discharge power is compared with measurements of the total power output of the generator made by a power meter. Results concerning power consumption and impedance in argon and silane discharges are presented as a function of the excitation voltage and the pressure. In both cases there is a discharge impedance drop, for higher voltage or pressure, which leads to higher power consumption in the discharge. The measurements show that only a small, nonconstant part of the power is consumed in the discharge, whereas, the inclusion of resistive loses leads to more accurate results. The mechanisms of the discharge impedance drop are further discussed in terms of their relation to microscopic plasma phenomena and quantities. © *1996 American Vacuum Society.*

I. INTRODUCTION

Capacitively coupled low-pressure radio-frequency (rf) discharges are widely used for the deposition and etching of materials in thin film technology. The problem of accurate control of the macroscopic parameters is commonly encountered in all these plasma processes. This is particularly true for plasma chemical-vapor deposition (CVD), where the deposition rate and the qualitative characteristics of the deposited films depend on the exact plasma conditions.[1] This includes besides pressure, flow rate, temperature, and power, other parameters like the discharge geometry or the deposition history which in turn can affect the way power is coupled to the discharge, because of the change in transfer impedance.[2] Therefore, the investigation and control of the electrical properties of such discharges can give an insight in these aspects and help in further understanding and controlling the process. Furthermore, it can reveal useful relations between those parameters and microscopic plasma phenomena, like ionizing or decomposing collisions and electron heating mechanisms, and quantities like charge carrier densities and energies.[3–5]

Several methods have been proposed in the past, for the determination of the impedance of a gas discharge and the power that is actually consumed by it. The experimental techniques can be grouped, based on the measured physical quantities, in four categories: (a) output impedance measurements, (b) in line power meter measurements, (c) voltage and current measurements, and (d) calorimetric determinations.

In the first case, the discharge impedance can be obtained as the complex conjugate of the output impedance of a correctly tuned matching network.[6–8] This can be measured with an impedance bridge, or calculated from the network components, after extinguishing the discharge. For this technique to work, the losses in the matching network should be small, however, this is not true in most of the practical cases.[9]

Other techniques use in line power meters to measure the dissipated power in the discharge.[10,11] For this purpose, the generator output power is measured once with the discharge on, and another with the discharge off, for the same driving voltage. The power dissipated by the discharge is then calculated by the difference of these two quantities. This subtractive method can give further information about the discharge impedance, if the settings of a proper matching network are recorded.

Other methods use voltage and current measurements. The main difficulty in these methods is, the fact that the voltage and current measurements are made outside the reactor. However, the existence of a stray impedance between the point of measurement and the electrode surface interferes with the direct measurement of the plasma impedance. In order to overcome this inconvenience, some studies have used dummy loads for determining the stray impedance of the reactor or embedding network.[12,13] The connection of the dummy load between the electrodes however, introduces a source of error because the rf contact conductivity changes each time the contacts are reconnected. A two-port circuit model is alternatively used for the stray impedance characterization of the reactor itself,[13,14] or the matching unit and the reactor as a whole.[9] In this approach, the network of parasitics is treated as a black box, containing arbitrary resistive, inductive, and capacitive elements. Other studies have used variations of these techniques to correct for the stray impedance or to avoid interference from it.[15–18] In this

context, the GEC group has proposed a general method for the electrical characterisation of gas discharges in the GEC reference cell;[19] in their analysis, however, they do not take into consideration any resistive losses.

A pair of methods use calorimetric techniques for calculating the power losses on the matching network and the cables and subtract this value from the total power measured with an in-line power meter with the discharge in operation.[18,20] In this way, the power dissipated by the discharge can be calculated, but no data for its impedance can be extracted, while the methods are laborious and difficult to apply in usual discharge chambers especially in low power conditions.

The major requirements of an impedance and power measurement technique are: relative simplicity and applicability to most of the existent experimental systems. Moreover, the method should provide information, without interrupting the process if control is to be pursued. This excludes methods that need special reactor configurations or do not provide information about the reactor and discharge impedance. This is particularly true for discharges of film depositing gases which can alter the discharge characteristics by covering the conductive surfaces.[21]

In this study, impedance and power measurements were performed in a parallel-plate CVD reactor. An electrical equivalent circuit accounting for the stray impedance of the cell is used in order to convert the current and voltage waveforms measured outside the chamber, to equivalent waveforms at the rf electrode. An inductive shunt circuit is then externally connected for increasing accuracy. The electrical circuit is complemented in order to account for power losses due to stray resistance both in the shunt circuit and the cell itself. This is done in a simple way which both increases the accuracy over previous approaches, while making the method applicable to all plasma deposition reactors without the need for a special chamber construction. In this case, results obtained from different, completely characterized, systems can be compared. Power and impedance measurements for discharges of noble and reactive gases are presented and discussed.

II. EXPERIMENT

The experimental arrangement used in our present work is schematically shown in Fig. 1. The design of the cell is described in detail elsewhere.[22] Briefly the cell is a 160 mm wide, parallel plate discharge chamber with 55 mm in diam electrodes. The electrodes are cylindrically symmetric and their distance can be continuously adjusted from 0 to 70 mm. One of the two electrodes is powered by an ENI ACG-3 13.56 MHz rf generator isolated with an L-type matching network. The rf electrode is surrounded by a grounded shield. A FCC model F-35-1 current probe and a Hameg model HZ 53 100:1 attenuating voltage probe were attached to the power lead after the matching network as close as possible to the electrode. The voltage and current signals were recorded by a Lecroy model 9400 digital oscilloscope and then transferred to a computer for Fourier analysis. The

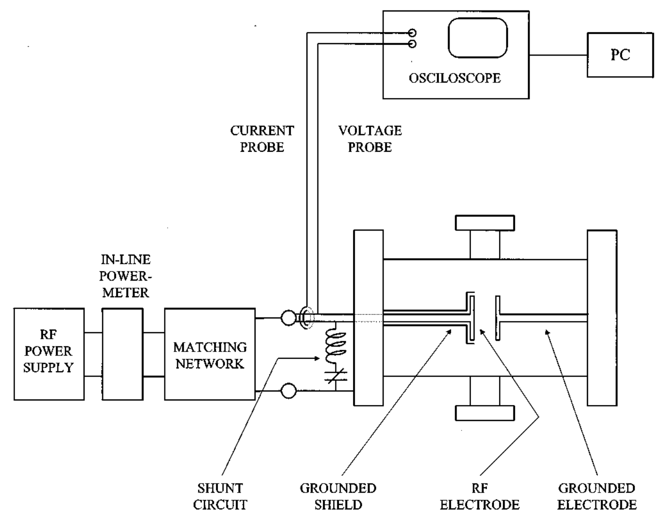

FIG. 1. Schematic diagram of the plasma chamber and the electrical connections used for power and impedance measurements.

amplitude and phase of the five first harmonic components were extracted by a discrete Fourier transform technique. The total power output of the generator is measured by a BIRD 4410A thruline wattmeter.

The determination of the voltage and current waveforms at the rf electrode involves the calibration of the probes for propagation delay errors, the construction of an equivalent circuit accounting for the components of the cell, the connection of a shunt circuit for minimizing the displacement currents generated by the stray capacitance of the cell, and the experimental determination of the values of the actual cell-shunt circuit components. The method is described in the following paragraphs.

III. PROBE CALIBRATION

In order to perform accurate electrical measurements using voltage and current probes, one has to take into account the propagation delays in the probes and the probe cables that connect them to the oscilloscope. In radio frequencies these systematic errors can be significant, as the signal requires a considerable fraction of the rf time cycle to traverse a cable with ordinary length. The shift of a waveform in the time domain diagram affects only the phase in the frequency domain diagram of a Fourier transform. More specifically, a time delay t will shift the phase of a signal at frequency f by an amount φ, where $\varphi=360°ft$.

The method used for determining the phase shifts of the voltage and current probes,[14] is briefly described here—the output of the voltage probe was connected to one channel of the oscilloscope and the probe tip was attached to the other channel. Then, a sinusoidal reference signal was driven to the probe tip. The phase difference between the two channels determined the voltage probe phase error. The same was repeated for several frequencies in order to determine the phase error at higher harmonics of the 13.56 MHz fundamental.

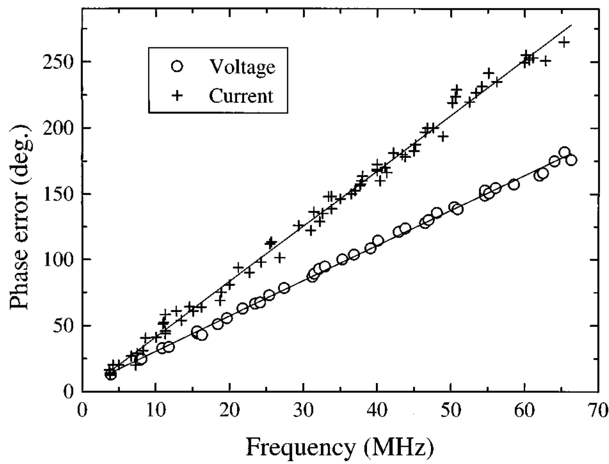

FIG. 2. Phase errors of voltage and current probes, due to propagation delays, as a function of frequency. Both probes are dispersionless, i.e., the time delay is independent of frequency, or the phase delay directly proportional to frequency. All measurements in this work were corrected for these systematic errors.

The phase error of the current probe was indirectly determined by measuring the phase difference between current and voltage in purely capacitive and inductive loads. With the phase error of the voltage probe corrected, as described above, one can determine the current probe phase error by comparing the measured impedance phase (the phase of the voltage relative to the current) to the expected values: $-90°$ for capacitive loads and $+90°$ for inductive loads. The phase errors of voltage and current probes are plotted against frequency in Fig. 2, where data from ten different loads have been used for the current probe. The vertical spread of the data for the current probe curve is due to resistive parasitics in the loads that cause the impedance phase to deviate from the ideal values of $\pm 90°$. Since the data for the two probes can be well fitted with a straight line, it means that the probes are dispersionless (the phase delay is directly proportional to frequency). The slope of these lines gives a delay time of 7.3 ns for the voltage probe, and 11.4 ns for the current probe.

IV. ELECTRICAL MEASUREMENTS

In order to determine the electrical properties of a discharge, one has to know the values of current and voltage inside the chamber at all surfaces in contact with the plasma. In most impedance analysis and investigations of potential distribution in discharges, however, scientists consider two surfaces in contact with the plasma; the rf electrode and the grounded one. They also consider that the ground potential is held by the grounded electrode, the chamber walls and the grounded shield of the rf electrode. However, although all these metallic surfaces are in electric contact, they are not all at the same voltage at any instant of the rf cycle. Voltage drops with amplitude of 1%–2% of the rf driving voltage, have been measured between points that are supposed to be both ''grounded.'' This has been also observed by others[9] and is due to the extreme difficulty of getting a proper ground connection at radio frequencies. The reason is that even a small inductance, L, gives a significant impedance, $jL\omega$, and attention should be paid to the way the connections are made between grounded conductors. This introduces voltage drops not only on the grounded parts but also on the powered ones. Therefore, a stray impedance is present in the cell from the point of measurement to the point of interest. In the present study, the current flowing through the powered electrode into the plasma and the voltage on the electrode surface with respect to the grounded shield are used for the electrical characterization. The measurement of these quantities, however, is not straightforward. Due to the stray impedance of the cell, the current and voltage waveforms at the point outside the cell, where the probes are physically located, will differ from the actual waveforms at the surface of the powered electrode. This is primarily due to the inductance between the measurement point and the electrode and the capacitance between the electrode and the ground shield. A simplified $L-C$ (inductance–capacitance) electrical circuit (Fig. 3) is used in order to determine the cascade matrix of the network of parasitics between the measurement point and the surface of the powered electrode.

The electrical analysis of this circuit shows that the nth harmonic component of the complex electrode voltage $\mathbf{V_{en}}$ and current $\mathbf{I_{en}}$ are related to the nth harmonic component of the measured complex voltage $\mathbf{V_n}$ and current $\mathbf{I_n}$ by

$$\mathbf{V_{en}} = \mathbf{V_n} - j\omega_n L \mathbf{I_n}, \tag{1}$$

$$\mathbf{I_{en}} = (1-\omega_n^2 LC)\mathbf{I_n} - j\omega_n C \mathbf{V_n}, \tag{2}$$

where the subscript n refers to the nth harmonic $\omega_n = n\omega$, and ω is the angular frequency of the fundamental driving frequency ($\omega = 2\pi\ 13.56\times 10^6$ rad/s). For the actual cell parameters, however, the parasitic currents are large and the corrected values are very sensitive to small errors in the measured values. The electrode current $\mathbf{I_{en}}$ is a very small quantity in relation with the measured current $\mathbf{I_n}$. This is because the actual electrode current results as the difference between two large numbers: the measured current, minus the displacement current $j\omega C\mathbf{V_n}$ due to the capacitance between the rf electrode and the grounded shield.

To avoid this difficulty, a shunt circuit consisting of an inductor L_s and an air variable capacitor C_s, was connected between the power lead and the chamber ground at a point between the current probe and the chamber.[19] The shunt has a net inductive impedance at 13.56 MHz and its purpose is to cancel at that frequency the net capacitive reactance of parasitics in the cell. The capacitor is used for ease in tuning the shunt and to maintain capacitive coupling to the cell. The shunt circuit is tuned by exciting the empty cell (with no discharge) with a sinusoidal voltage at 13.56 MHz and adjusting the shunt capacitor C_s until the measured current is nulled. In this situation the net reactance, $j\omega L_s + 1/j\omega C_s$ of the shunt cancels the net reactance $j\omega L + 1/j\omega C$ of the cell's equivalent circuit:

$$j\omega L_s + \frac{1}{j\omega C_s} = -\left(j\omega L + \frac{1}{j\omega C}\right). \tag{3}$$

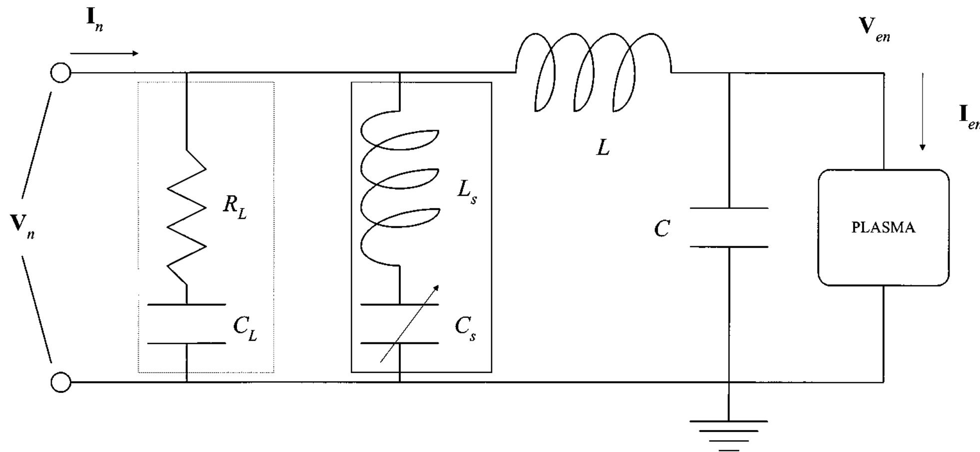

FIG. 3. The equivalent circuit for the determination of the cascade matrix of the network of parasitics. The $L-C$ circuit represents the cell parasitics, the L_s-C_s circuit (in the solid box) is the shunt circuit connected externally, and the R_L-C_L circuit (in the dotted box) accounts for resistive losses in the cell and shunt circuit.

With the shunt circuit connected, Eqs. (1) and (2) that transform the measured values $\mathbf{V_n}$ and $\mathbf{I_n}$ to the electrode ones $\mathbf{V_{en}}$ and $\mathbf{I_{en}}$ become:

$$\mathbf{I_{en}}=(1-\omega_n^2 LC)\mathbf{I_{Ln}}-j\omega_n C\mathbf{V_n}, \tag{4}$$

$$\mathbf{V_{en}}=\mathbf{V_n}-j\omega_n L\mathbf{I_{Ln}}, \tag{5}$$

where

$$\mathbf{I_{Ln}}=\mathbf{I_n}-\frac{j\omega_n C_s\mathbf{V_n}}{(1-\omega_n^2 L_s C_s)}. \tag{6}$$

The shunt and the cell however are not pure reactances. They have also stray resistive components which cause additional power losses upon them. Therefore, the shunt does not exactly null the measured current. It is observed that the current takes a minimum value in the tuned situation, that is not zero. The remaining residual current is $\approx$3.5% of the current without the shunt present. Although the cell itself has a small resistance, (the phase difference between the voltage and current without the shunt and in the absence of discharge is very close to $-90°$; at least for the first and second harmonic) by attaching the shunt circuit, additional and considerable ohmic parasitics are introduced. The large increase in precision made possible by the shunt is partly outweighed by the above disadvantage.

Measurement of this residual current has lead us to include in some way the stray resistive components of the cell-shunt at the equivalent electrical circuit. Namely, with the shunt properly tuned, the input impedance V_1/I_1 of the empty cell and shunt circuit was independent of the excitation voltage over the whole range 25 V$<V<$100 V. Moreover, this residual current was in phase with the voltage at the point of measurement with a deviation of $\pm 2°$ when the cell was driven with a sinusoidal voltage in this range of voltages. This behavior is equivalent as if the residual current flows, in parallel to the shunt circuit, from the rf power lead to the ground. This is taken into account by introducing a resistance R_L in the equivalent circuit parallel to the shunt (Fig. 4). In this way, one can say that in the tuned situation, the reactant components of the cell-shunt circuit are nulled and the remaining residual current is due to the resistance which draws the measured current parallel from the rf power lead to the ground. The additional capacitor C_L is introduced at the specific point of the equivalent circuit to justify the existence of the dc bias of the powered electrode which is due to the capacitive coupling of the power generator to the cell. Its capacitance is considered to be infinite and is not involved in the calculations (it has zero impedance $1/j\omega C_L$, and thus no contribution to phase difference between the voltage and the residual current).

Thus, taking into consideration R_L and C_L, the final relations that convert the measured values to the equivalent values at the electrode are given by the relations:

$$\mathbf{V_{en}}=\mathbf{V_n}-j\omega_n L\mathbf{I_{Ln}}, \tag{7}$$

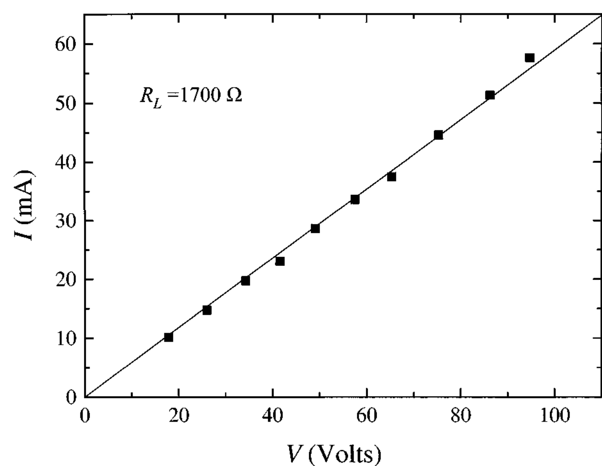

FIG. 4. Plot of the residual current as a function of the driving voltage at 13.56 MHz, with the shunt connected and tuned for minimum current. The measurements are made in the absence of plasma. The inverse of the slope of the forced to zero crossing line gives the value of the resistance R_L.

$$\mathbf{I_{en}} = (1-\omega_n^2 LC)\mathbf{I_{Ln}} - j\omega_n C\mathbf{V_n}, \tag{8}$$

where

$$\mathbf{I_{Ln}} = \mathbf{I_n} - \frac{\mathbf{V_n}}{R_L} - \frac{j\omega_n C_s \mathbf{V_n}}{(1-\omega_n^2 L_s C_s)}. \tag{9}$$

The dissipated power P can be then calculated from $\mathbf{V_{en}}$ and $\mathbf{I_{en}}$ by:

$$P = \frac{1}{2}\sum_{n=1}^{5} V_{en} I_{en} \cos \varphi_{en}, \tag{10}$$

where φ_{en} is the phase of $\mathbf{V_{en}}$ relative to $\mathbf{I_{en}}$, and V_{en} and I_{en} are the magnitudes of $\mathbf{V_{en}}$ and $\mathbf{I_{en}}$, respectively. Only the first five harmonics exist in current waveform, at least with considerable amplitude, when the plasma is present.

V. CIRCUIT COMPONENTS

If one can determine the exact values of the electrical components that are involved in the equivalent circuit, then the measured values, $\mathbf{V_n}$ and $\mathbf{I_n}$ can be converted to the equivalent ones at the surface of the rf electrode, $\mathbf{V_{en}}$ and $\mathbf{I_{en}}$. The values for L and C were determined by measuring the impedance of the cell at the fundamental and the second harmonic without the shunt circuit. These measurements were made by exciting the cell without discharge with a 13.56 MHz arbitrary wave signal. Voltage and current were recorded with the probes connected at the same point that would later be used for plasma measurements. The fundamental and second harmonic of voltage and current waveforms were deduced by Fourier analysis of the measured signals. The cell's impedance phase (the phase of the voltage relative to the current, in the absence of plasma) at these two frequencies was $-88°$–$-89°$ indicating the net capacitive reactance of the cell and the very small residual component that has been already mentioned. The impedance of the cell was then determined by the ratio of voltage to current:

$$\mathbf{Z_n} = \frac{\mathbf{V_n}}{\mathbf{I_n}}. \tag{11}$$

According to the $L-C$ equivalent circuit (Fig. 3) for the cell parasitics, the impedance of the cell is given by:

$$\mathbf{Z_n} = jn\omega L + \frac{1}{jn\omega C}. \tag{12}$$

L and C can be determined by solving the equations that give the cell's impedance at the fundamental and second harmonic:

$$\frac{\mathbf{V_1}}{\mathbf{I_1}} = j\omega L + \frac{1}{j\omega C} \quad \text{and} \tag{13}$$

$$\frac{\mathbf{V_2}}{\mathbf{I_2}} = j2\omega L + \frac{1}{j2\omega C}. \tag{14}$$

For the determination of the shunt circuit components, the shunt circuit was connected and tuned. The capacitance C_s was measured with a capacitance meter, after being isolated from the circuit. The inductance L_s was then calculated by using Eq. (3). Finally, the resistance R_L was obtained by the ratio V_1/I_1 of the driving voltage to the residual current, with the shunt circuit in the tuned position. In Fig. 4, this residual current at 13.56 MHz is plotted as a function of driving voltage. The inverse of the slope of the best fitted line which is forced to zero crossing, gives the value of this resistance.

TABLE I. Equivalent circuit components' values.

C (pF)	L (nH)	C_s (pF)	L_s (nH)	R_L (Ω)
129	18	187	1786	1700

Note that the addition of this resistance does not disturb the determination of the values of C, L, C_s, and L_s, because it has been separated from the reactant components of the cell-shunt circuit, which are fully nulled in the tuned situation. The value of R_L obtained in this way at 13.56 MHz is used for the higher harmonics without taking into account that rf resistances are frequency dependent due to the skin effect. The current at higher harmonics that flows through the resistance R_L, however, is negligible, as the amplitude of the measured voltage at higher harmonics is less than 1% of that of the fundamental at all cases.

For voltages greater than 100 V in amplitude, the ratio V_1/I_1 deviated from the calculated value of R_L in the range 25 V$<V<$100 V and, therefore, for these voltages this equivalent circuit could no more account for the stray impedance of the cell-shunt circuit. Moreover, in this case the phase difference between the residual current and the voltage was not in the range $0°\pm2°$ and could not be considered "in phase" anymore. The phase difference and the ratio V_1/I_1 in these cases was time dependent indicating that, in these voltages, power dissipation in the parasitics produced a significant rise in the temperature of connection cables, thus altering both the value of the resistance R_L and the impedance phase of the cell-shunt circuit. The value of R_L, for voltages below 100 V, remained unchanged even if the discharge was in operation for hours and the measurement made immediately after extinguishing the discharge.

The values for the electrical components involved in the equivalent circuit, which is used for the characterization of the stray impedance of the cell-shunt circuit, are shown in Table I.

VI. RESULTS AND DISCUSSION

Power and impedance measurements have been performed for a variety of conditions in film depositing and non film depositing discharges. The main discharge conditions are given in Table II.

As it is shown in Fig. 5, which presents the power consumed in the discharge, as a function of the peak-to-peak rf voltage, for various pressures of argon or silane, there is an increase of the power consumed in the discharge with increasing V_{pp} or pressure. The effect of V_{pp} is more pronounced at higher pressures. This increase is not linear with either V_{pp} or pressure, as it can be seen also in the subsequent Fig. 6. An increase of the power consumed in the

TABLE II. Range of experimental discharge conditions for argon and silane.

	P (mTorr)	V_{pp} (V)	f (sccm)	D (mm) electrode diameter	d (mm) interelectrode distance
Ar	50–800	50–200	10–20	55	25
SiH_4	35–100	75–200	10–20	55	25

discharge can be a result of the increase in the net current flow, and of a change of the discharge impedance. These factors depend mainly on the magnitudes of the reactive and capacitive components of the discharge that can be translated into values of the microscopic parameters like the electron and ion density and energy, the number of collisions, and the characteristics of the sheaths. However, since the current flow is dependent on impedance, the picture provided by Fig. 5 is too general to give further insight for these microscopic parameters.

The plot presented in Fig. 6, gives also evidence for the existence of different discharge regimes, by the appearance of a small maximum at around 100 mTorr and of a tendency for saturation at higher pressures. Both features are more pronounced at higher excitation voltages. At low pressures, the discharge is spread in the entire chamber, coming in contact with all the grounded surfaces. When pressure increases the discharge is more confined in the interelectrode space due to the lower mean free path associated with a larger

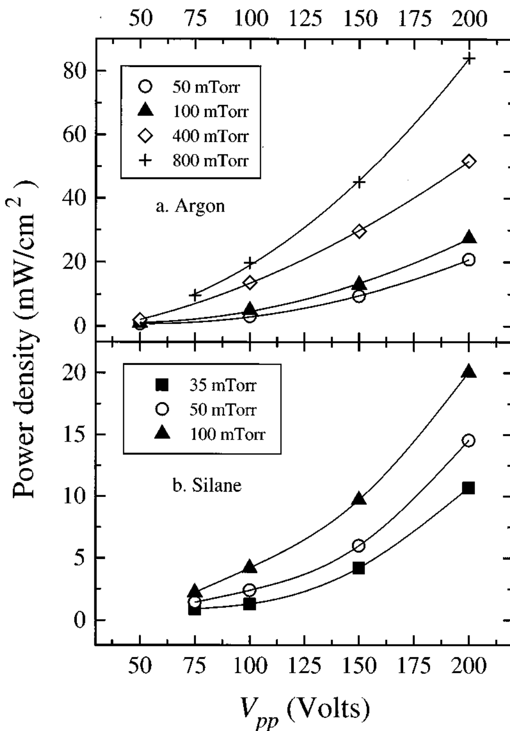

FIG. 5. The power density consumed in the discharge as a function of the rf peak-to-peak voltage V_{pp} for various pressures of (a) argon and (b) silane. The power P is divided by the surface area of the rf electrode to give power density in mW/cm^2.

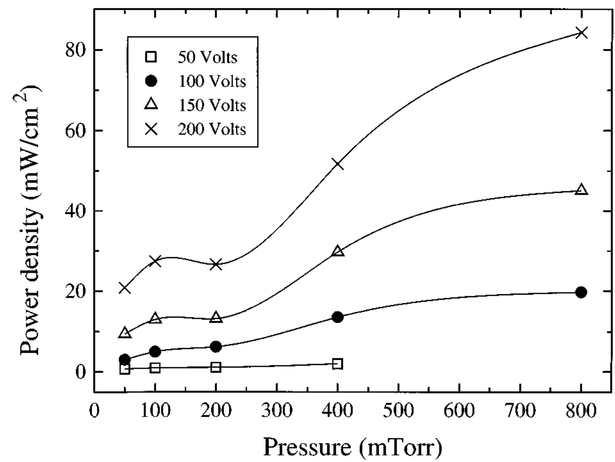

FIG. 6. The power density as a function of argon pressure for 50, 100, 150, and 200 V peak-to-peak rf driving voltages.

number of collisions. On the other hand, at even higher pressures the current flowing through the discharge is limited by the given ionization rate at a specific excitation voltage. In any case, there is need for additional analysis in order to give a full explanation of the significance of the previous figures. It is clear, however, that one can vary the power consumed by the discharge not only by varying the V_{pp} but also by varying the chamber pressure at a constant V_{pp}. Moreover, the discharge power is a function of the nature of the gas and other discharge parameters as it is shown in Fig. 5.

In contrast to the measurements presented, the total power measured by the SWR bridge, before the matching network, shows small variations of the order of ±20% when increasing pressure, while the power really consumed in the discharge changes more than four times, for higher V_{pp}. The reason for this behavior is that most of the power output of the generator is consumed in the matching network and the stray impedance of the reactor. Thus, it is interesting to see the relation of the actual power, P, dissipated in the discharge to the nominal power, P_N, measured by the power meter, for the same conditions, as it is shown in Fig. 7. This plot shows that there is no constant relation between P and P_N. The actual power is a small non constant fraction of the total power, although again the amount of power consumed in the discharge is higher at higher V_{pp} and pressures. This is due to the fact that plasma impedance is changing, and thus a larger amount of power is transferred from the power generator to the discharge. In general, one can write for the output power of the generator:

$$P_N = P_L + P = \frac{V^2}{2Z_L^2} R_L + \frac{V^2}{2Z_P^2} R_P = \frac{V^2}{2} \frac{R_P Z_L^2 + R_L Z_P^2}{Z_L^2 Z_P^2}, \tag{15}$$

$$\frac{P}{P_N} = \frac{R_P Z_L^2}{R_P Z_L^2 + R_L Z_P^2} \tag{16}$$

thus:

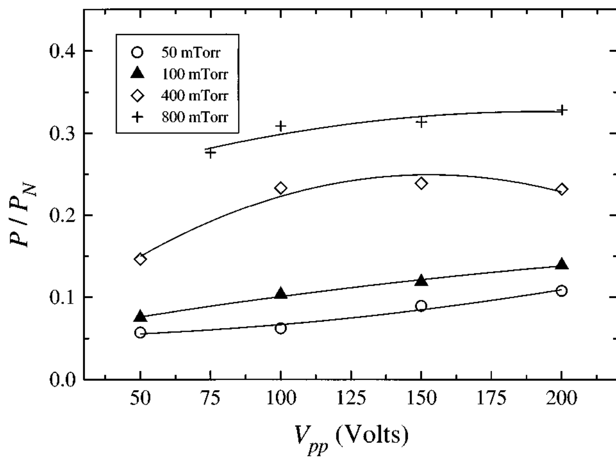

FIG. 7. The ratio of the power P, actually consumed in the discharge, to the nominal power P_N, as a function of V_{pp} for various argon pressures. The nominal power is measured with an in line power meter before the matching network and includes, besides the power consumed in the discharge, the power losses in the matching network and the cell-shunt circuit.

$$\frac{P}{P_N} \rightarrow 1 \quad \text{for } R_P Z_L^2 \gg R_L Z_P^2,$$

$$\frac{P}{P_N} \rightarrow 0 \quad \text{for } R_P Z_L^2 \ll R_L Z_P^2,$$

where, V is the amplitude of the driving voltage, P_N is the total power, P_L, Z_L, and R_L refer to the matching network and cables, the cell and the shunt, while P, Z_p, and R_p refer to the discharge.

These relations are true for the case of in parallel connection of both the discharge and the matching, shunt and cell components, and gives a qualitatively good approximation of the real situation. This can be seen in Fig. 8, where the relative amounts of power consumed in the discharge, the shunt and cell, and the matching and cables, as well as the total power, are presented together with the discharge impedance. It is observed here that the total power is changing to the

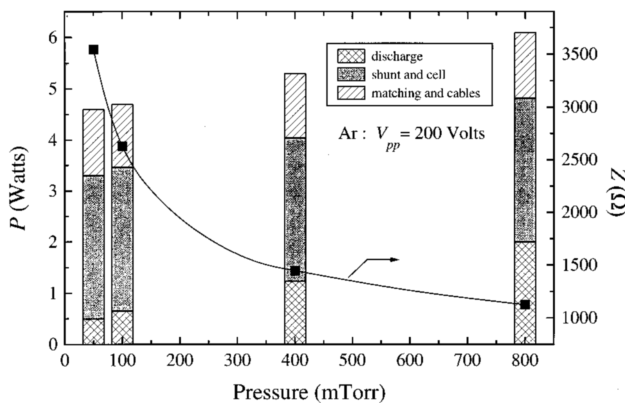

FIG. 8. Power consumption in the discharge, shunt and cell, and matching network and cables, as a function of argon pressure. The rf peak-to-peak voltage is kept constant at 200 V. The dependence of the discharge impedance Z upon pressure is also shown for comparison.

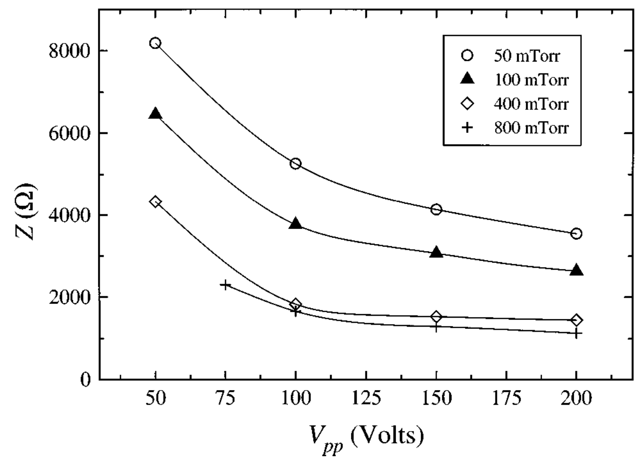

FIG. 9. The discharge impedance Z as a function of the rf peak-to-peak voltage V_{pp} for various argon pressures.

extent that pressure is changing while the amounts of power consumed in the matching and cables, or the cell and the shunt remain constant. The observed decrease of the discharge impedance is in agreement to the increase of the power consumed in the discharge, according to Eq. (16). This figure presents very well the advantages of the method used in this work over previous methods that did not take into account resistive losses. Namely, in this case the amount of power consumed in the shunt and cell would be attributed to the discharge, giving an erroneously high discharge power consumption. Moreover, the elimination of the resistive component from the equivalent circuit (Fig. 3) can give in some cases, at least for this particular system, positive plasma impedance phase values. This would indicate that the discharge presents an inductive instead of capacitive reactance. Note that the inclusion of the resistive component in the equivalent circuit makes the method more generally applicable even for the cases when, due to different chamber construction characteristics, the value of this resistance is small.

The discharge impedance shown in Fig. 8, drops at higher pressures. The same is true for the variation of impedance with V_{pp}, as shown in Fig. 9. The value of the impedance at 13.56 MHz is given by the ratio of the fundamental component of the voltage amplitude, to the fundamental component of the current amplitude, V_{e1}/I_{e1} at the rf electrode. The complex discharge impedance at 13.56 MHz is given by the equation:

$$\mathbf{Z} = \frac{\mathbf{V_{e1}}}{\mathbf{I_{e1}}} = \frac{V_{e1}}{I_{e1}} e^{j\varphi_{e1}} = R + jX, \tag{17}$$

where φ_{e1} is the phase of the fundamental electrode voltage $\mathbf{V_{e1}}$, relative to the fundamental electrode current, $\mathbf{I_{e1}}$, R is the real part or the discharge resistance, and X the imaginary part, or the discharge capacitive reactance. The real and the imaginary part are given by the following equations:

$$R = Z \cos \varphi_{e1} = \frac{V_{e1}}{I_{e1}} \cos \varphi_{e1}, \tag{18}$$

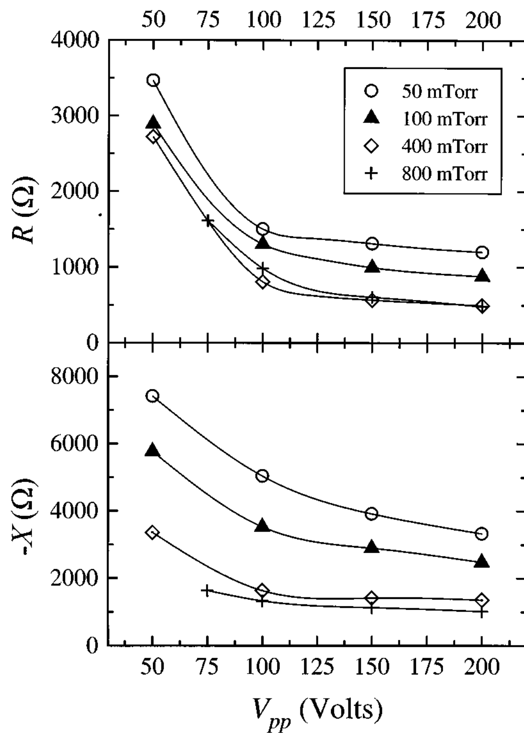

FIG. 10. The real R and the imaginary part X of the discharge impedance $Z=R+jX$, as a function of the rf peak-to-peak voltage V_{pp} for various argon pressures. The real part is the resistive component of the discharge impedance, responsible for the power consumption. The imaginary part stands for the reactance and is always negative indicating the capacitive character of the discharge.

$$X=Z \sin \varphi_{e1}=\frac{V_{e1}}{I_{e1}} \sin \varphi_{e1}. \quad (19)$$

It can be observed in Fig. 10 that both values given by Eqs. (18) and (19) decrease with increasing V_{pp} or pressure. In order to interpret this behavior one can adopt a simple electrical model for the discharge, consisting of a capacitance accounting for the sheaths, and an in series resistance for the consumption of power in the bulk and the sheaths. The power consumption is due to the acceleration of plasma electrons by the sheath field or the bulk plasma field, and the acceleration through the sheath of ions and secondary electrons.[16,23] The decrease of the capacitive reactance is due to an increase of the sheath capacitance as both sheaths become smaller at higher pressures,[24] while the decrease of the resistance is due to the increase in the electron energy and density at higher V_{pp} and pressures, respectively. Therefore, as it is expected, the discharge impedance will drop in both cases, leading to better power coupling, although the mechanism is different in each case.

In order to better illustrate the two cases, one can use the representation of the complex impedance vector for certain impedance values. In Fig. 11(a), is presented the case of V_{pp} increase for Ar at 100 mTorr, while in Fig. 11(b) the case of pressure increase for Ar discharge at $V_{pp}=100$ V. In the first case, the discharge is becoming more capacitive, whereas, in the second case more resistive. The same thing can be easily

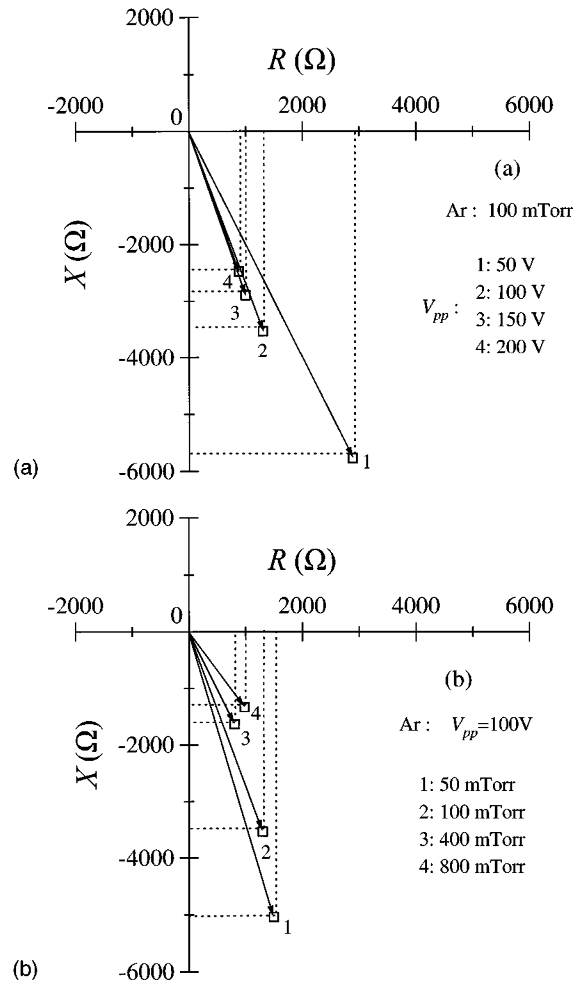

FIG. 11. The discharge impedance vector in the complex plane. The magnitude of the directed line segment to the point defines the magnitude while the angle with the real axis defines the phase angle of the complex discharge impedance Z. The abscissa defines the reactance of the discharge while the ordinate the resistance. (a). The dependence of the complex discharge impedance upon rf peak-to-peak voltage for an 100 mTorr argon discharge. (b). The dependence of the complex discharge impedance upon pressure for a constant 100 V rf peak-to-peak voltage.

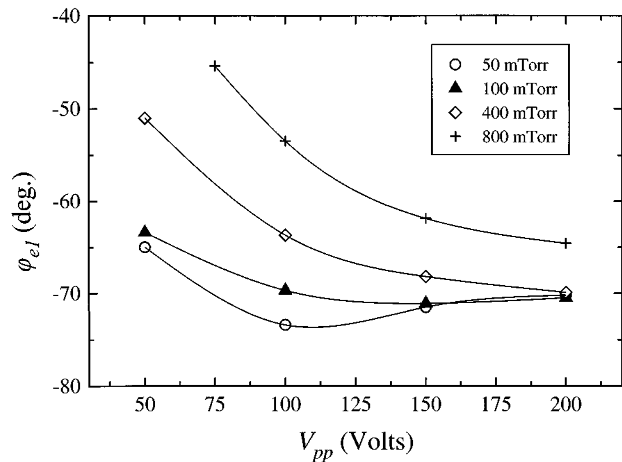

FIG. 12. The discharge impedance phase φ_{e1} as a function of rf peak-to-peak voltage for various argon pressures.

seen in the plot of the impedance phase versus V_{pp} for different pressures (Fig. 12). This is because when increasing V_{pp}, the increase of the electron energy results to a higher ionization rate which decreases the discharge resistance. At the same time, the ion energy and the sheath potential are increased leading to more confined sheaths,[25] higher sheath capacitance and thus smaller sheath capacitive reactance. The higher sheath field will increase the amount of power consumed for the acceleration of ions and secondary electrons in the sheath. In the case of higher pressures, the smaller mean free path of the electrons leads to smaller sheath dimensions and thus to higher sheath capacitance while the higher number of charge carriers leads to a decrease of the resistance.

VII. SUMMARY

A power measurement technique, together with results concerning argon and silane discharges, was presented. The novelty in this method consists in the inclusion of a resistive component, accounting for power losses in the cell and the shunt, in the equivalent circuit used for the transformation of the measured wave forms to equivalent wave forms at the rf electrode. The results presented show that the method is far more accurate than previous approaches, while it is more generally applicable. The results obtained for argon and silane discharges show evidence of different discharge regimes depending on pressure. The power coupling to the discharge is sensitive to the variation of both the discharge excitation voltage and pressure. The method can be used efficiently for controlling the deposition conditions of thin films with reproducible properties.[26]

[1]P. Kounavis, D. Mataras, N. Spiliopoulos, E. Mytilineou, and D. Rapakoulias, J. Appl. Phys. **75**, 1599 (1994).
[2]K. Ukai and K. Hanazawa, J. Vac. Sci. Technol. **16**, 385 (1979).
[3]N. Spiliopoulos, S. Stamou, D. Mataras, and D. Rapakoulias, *Proceedings of the 12th International Symposium on Plasma Chemistry, Minneapolis 1995*, edited by J. V. Heberlein, D. W. Ernie, and J. T. Roberts (University of Minnesota, Minneapolis, Minnesota, 1995), Vol. 4, p. 1927.
[4]A. J. van Roosmalen and P. J. Q. van Voorst Vader, J. Appl. Phys. **68**, 1497 (1990).
[5]A. M. Pointu, J. Appl. Phys. **60**, 4113 (1986).
[6]J. S. Logan, N. M. Mazza, and P. D. Davidse, J. Vac. Sci. Technol. **6**, 120 (1969).
[7]A. J. van Roosmalen, Appl. Phys. Lett. **42**, 416 (1983).
[8]D. B. Ilic, Rev. Sci. Instrum. **52**, 1542 (1981).
[9]B. Andries, G. Ravel, and L. Peccoud, J. Vac. Sci. Technol. A **7**, 2774 (1989).
[10]C. M. Horwitz, J. Vac. Sci. Technol. A **1**, 1795 (1983).
[11]V. A. Godyak and R. B. Piejak, J. Vac. Sci. Technol. A **8**, 3833 (1990).
[12]S. E. Savas, D. E. Horne, and R. W. Sadowski, Rev. Sci. Instrum. **57**, 1248 (1986).
[13]J. W. Butterbaugh, L. D. Baston, and H. H. Sawin, J. Vac. Sci. Technol. A **8**, 916 (1990).
[14]M. A. Sobolewski, J. Vac. Sci. Technol. A **10**, 3550 (1992).
[15]W. G. M. van den Hoek, C. A. M. de Vries, and M. G. J. Heijman, J. Vac. Sci. Technol. B **5**, 647 (1987).
[16]C. Bohm and J. Perrin, J. Phys. D: Appl. Phys. **24**, 865 (1991).
[17]P. Bletzinger and M. J. Flemming, J. Appl. Phys. **62**, 4688 (1987).
[18]C. Beneking, J. Appl. Phys. **68**, 4461 (1990).
[19]P. J. Hargis, Jr., K. E. Greenberg, P. A. Miller, J. B. Gerardo, J. R. Torczynski, M. E. Riley, G. A. Hebner, J. R. Roberts, J. K. Olthoff, J. R. Whetstone, R. J. van Brunt, M. A. Sobolewski, H. M. Anderson, M. P. Splichal, J. L. Mock, P. Bletzinger, A. Garscadden, R. A. Gottscho, G. Selwyn, M. Dalvie, J. E. Heidenreich, J. W. Butterbaugh, M. L. Brake, M. L. Passow, J. Pender, A. Lujan, M. E. Elta, D. B. Graves, H. H. Sawin, M. J. Kushner, J. T. Verdeyen, R. Horwath, and T. R. Turner, Rev. Sci. Instrum. **65**, 140 (1994).
[20]J. A. G. Baggerman, R. J. Visser, and E. J. H. Collart, J. Appl. Phys. **76**, 738 (1994).
[21]N. Spiliopoulos, D. Mataras, and D. Rapakoulias, *Proceedings of the 12th International Symposium on Plasma Chemistry, Minneapolis 1995*, edited by J. V. Heberlein, D. W. Ernie, and J. T. Roberts (University of Minnesota, Minneapolis, Minnesota, 1995), Vol. 4, p. 2143.
[22]D. Mataras, S. Cavadias, and D. Rapakoulias, J. Vac. Sci. Technol. A **11**, 664 (1993).
[23]Ph. Belenguer and J. P. Boeuf, Phys. Rev. A **41**, 4447 (1990).
[24]W. B. Pennebaker, IBM J. Res. Develop. **23**, 16 (1979).
[25]V. A. Godyak and A. S. Khanneh, IEEE Trans. Plasma Sci. **PS-14**, 112 (1986).
[26]N. Spiliopoulos, S. Stamou, D. Mataras, and D. Rapakoulias, *Proceedings of the 13th EC Photovoltaic Solar Energy Conference*, edited by W. Freiesleben, W. Palz, H. A. Ossenbrink, and P. Helm (H. S. Stephens and Associates, Nice, France, 1995), Vol. 1, p. 292.